mathematics

MDPI

Article

Unraveling Nonlinear Wave Dynamics in Hydraulic Engineering: Symbolic Neural Network Solutions for the (3+1)-Dimensional P-Type Model

Qi-Yun Sun [1] and Wen-Feng Feng [2,*]

[1] Aulin College, Northeast Forestry University, Harbin 150040, China; sqyzyyx@nefu.edu.cn
[2] Embodied Intelligence College, Henan Polytechnic University, Jiaozuo 454003, China
* Correspondence: fengwf@hpu.edu.cn

Abstract

In this paper, the nonlinear wave dynamics of the (3+1)-dimensional P-type model are investigated using a symbolic neural-network-based hybrid technique. The model is considered in the context of nonlinear wave propagation, which is of practical importance in different areas. This approach combines the modified generalized Riccati equation mapping method with a neural network structure, where each neuron in the first hidden layer represents a Riccati-based activation function, which allows the construction of new physics-based trial solutions. This approach allows the systematic generation of exact traveling wave solutions in space and time. Solutions including solitary waves, and periodic and localized pulses are obtained, which provide essential insight into the influence of model parameters on wave profiles and evolution in complex media. The dynamics of the waves are illustrated by two-dimensional, three-dimensional, and contour plots, which show the behavior of propagation, localization, and stability. The results demonstrate the method is feasible, efficient, and effective for studying high-dimensional nonlinear systems. This work not only extends the Riccati-based neural network approach to the model but also provides a platform for exploring nonlinear wave behavior in shallow-water flows and other hydraulic engineering problems.

Keywords: symbolic neural network; Riccati-based activation function; hydraulic engineering; solitons

MSC: 35Q51; 35C08

Check for updates

Academic Editors: Runfa Zhang, Zhongzhou Lan and Jianguo Liu

Received: 1 September 2026
Revised: 11 October 2026
Accepted: 13 October 2026
Published: 26 October 2026

Copyright: © 2026 by the authors. Licensee MDPI, Basel, Switzerland. This article is an open access article distributed under the terms and conditions of the Creative Commons Attribution (CC BY) license.

1. Introduction

Nonlinear wave phenomena have fascinated researchers in recent years for their fascinating characteristics and their deep connections to a wide range of contemporary fields of study. Whether in the ocean, optical fibers, plasma, biology, or elsewhere, nonlinear waves take the form of coherent structures that propagate energy and information in ways impossible to describe through linear theory [1]. Linear theory, despite its mathematical simplicity and historical significance, fails to explain the complex, often paradoxical, behavior of nature. The unexpected appearance of freak waves, dispersion-free propagation of solitons, steepening of waves, and chaotic dynamics are all beyond linear theories. This deficiency has stimulated a shift in paradigm to nonlinear models that can be used to capture higher-order effects; intrinsic nonlinearities; and the complicated interaction of dispersion, dissipation, and nonlinear steepening [2]. This has led to the fact that nonlinear science has

quickly become one of the most significant fields of contemporary study, transforming the way we understand both natural and artificial systems [3].

In addition, the nonlinear partial differential equations (NLPDEs) [4,5] are leading the revolution and are an essential mathematical instrument to represent a wide range of physical, industrial, and environmental processes. Their application is in fact prolifically wide ranging, including such different fields as fluid mechanics and optical fiber communications, quantum physics and geophysics, plasma physics and biology, ocean engineering, and hydraulic engineering. They are significant in the study of basic mechanisms like the wave propagation in open channels, coastal environments, offshore platforms (fluid-structure interactions), sediment transportation, surge waves development in estuaries, and the mechanisms of water distributed networks [6–8]. The variety of dynamics that can be exhibited by physical systems described by these equations is truly astonishing: pattern formation in a homogeneous medium, a cascade of scales in turbulence, coherent vortices in shear flow, and a sudden change of states with a small perturbation. The study of such complex flow phenomena is not just a question of interest but also has far-reaching consequences on the prediction of environmental trends, the design of resilient coastal and hydraulic infrastructure, the management of flood and tsunami processes, and the sustainability of water resources due to climate change changes. Such analytical and exact solution techniques provide the priceless and special view of the structure of these nonlinear models. Unlike purely numerical models that may hide the underlying physical processes and the sensitivities of the parameters, exact solutions reveal the underlying mathematical structure and the most important physical balances of the wave evolution, stability, and interactions. They are important in ensuring the accuracy of numerical models and the foundations of constructing more complex and realistic solutions of waves [9].

The (3+1)-dimensional P-type model is a highly flexible and essential model in higher-dimensional studies of nonlinear wave propagation in this huge space. This model extends to higher space and time dimensions, generalizing the spatial degrees of freedom of (1+1) and (2+1) space and time to (3+1) space and time and a more realistic and detailed model of more complex physical processes occurring on the real world of shallow water bodies in several directions, where waves can propagate, diffract, and focus concurrently. Based on the rich history of solitary wave theory and integrable systems, the (3+1)-dimensional P-type model has been the stimulus behind the creation and optimization of a huge number of analytical, algebraic, and symbolic computational methods, all aimed at building complete traveling wave and soliton solutions. It is within this fertile setting that the present study seeks to make its own contribution by attempting to stretch the limits between the abstract mathematical models and the real-world issues in hydraulic and coastal engineering.

The rapid advances in artificial intelligence, particularly deep learning and neural network algorithms, in recent years have significantly transformed scientific computing and nonlinear analysis. Such information-based methods have become powerful alternatives and, in many cases, complementary schemes to develop the knowledge of the complex and multifaceted properties of NLPDEs compared to the conventional numerical and analytical methods. Traditional methods, like finite difference, finite element and spectral discretizations, though powerful, may have serious difficulties in high-dimensional problems, complex geometries, or the notorious curse of dimensionality [10]. In comparison, the neural network techniques have the special ability to discover the solution of a problem by direct observation or even by direct observation of the equations model, without the time-intensive and expensive generation of meshes, the complicated discretization schemes, or the solvability criteria that tend to plague the traditional techniques. This ability to do a mesh-free, smooth, and trans-formative function approximation is, perhaps, their most significant and transformative feature [11]. Consequently, they perform well in

high-dimensional, costly, and complicated geometrical arrangements in which conventional solvers either falter or are prohibitively expensive. Deep neural networks are successful because of their remarkable approximation properties, which are founded on the universal approximation theory and exploited by their multi-layered hierarchical constructs capable of learning the complex nonlinear relationships with astounding accuracy. Deep learning models can capture the actual nonlinear physics of the system as opposed to the simplifying assumptions made about the solution, such as linearization or perturbation expansions. This renders them highly suitable in capturing steep gradients, sharp transitions, and coherent structures like solitons and rogue waves. Properly trained, these models are high-dimensional implicit function approximators that represent the underlying physics in the solution space, which learn low-dimensional latent representations that represent the physics [12]. The most recent disruptive technology in this field is the introduction of physics-informed neural networks (PINNs), which have now been able to extend the learning paradigm to the underlying PDEs, initial conditions, and boundary conditions and even conservation laws, appearing directly in the loss. Such smooth integration ensures both that the solution found is not merely an interpolation of the data but also that the underlying physics is respected, significantly improving its accuracy, explainability, and generalization (especially in situations where the data is sparse, noisy or partially missing) [13]. The learning of neural networks [14] is not merely approximation. These networks can be scaled and can easily use modern hardware accelerators like graphics processing units and tensor processing units, enabling solutions to be found at a scale that had never been considered before. The frameworks demonstrate superior behavior in unstructured and irregular domains, inherently able to support inverse problems with unknown parameters to be learned with the solution, and can be readily integrated with other methods like transfer learning, operator learning, and symbolic regression [15]. Besides this, neural networks with analytical algorithms known as symbolic neural networks, neuro-symbolic, or neuro-symbolic computing provide a novel quantum leap of capability by encoding the structure of closed form solutions in the network design itself and therefore generating interpretable, accurate, or approximate solutions, instead of black-box predictions. While these characteristics hold great promise, there remain some challenges. Challenges relating to training stability and hyperparameter tuning, convergence for stiff or multiscale PDEs, and the ability to transfer models to different physical settings are currently the subject of ongoing research [16–18]. The ability to address these issues is essential in the move towards deep learning becoming a mainstream technology to address important engineering challenges [19]. It is in this space—deep learning, symbolic computation and nonlinear physics—that the present work aims to leverage such cutting-edge approaches for modeling complex soliton dynamics in higher-dimensional water waves.

Moreover, the soliton solutions of NLPDEs play an important and unique role in most branches of science and engineering due to their remarkable stability in propagating over long distances without changing their shape, amplitude, and velocity. This special characteristic (shape-preserving during propagation) of nonlinear is deep and completely different from the linear wave equations, where such permanent localized wave forms are not found. In linear systems, all local disturbances of the wave must be dispersed, broadened, and damped. However, the emergence of a soliton is due to a precise and subtle balance between two effects; nonlinear steepening (which would tend to steepen and concentrate the wave) and dispersion (which would tend to smooth and spread out the wave) [20]. Where these effects are in balance, a coherent structure, which is localized, is formed, and this propagates unchanged, like a particle (though wave-like). This balance is built into the equations of most physically significant NLPDEs, where it results in the existence of soliton solutions that have been found and explored in detail in many places.

It has a close connection with soliton theory and engineering hydraulics and deals with topics both in wave physics and in the design of flood and navigation works. In coastal and open-channel hydraulics, solitary waves offer ideal models of many situations: the travel of tsunami waves in the ocean, the up-rushing undular bores in tidal estuaries, wakes of ships in narrow channels, and surge waves due to abrupt gate closures or dam wall failures. The profile, speed, and stability of solitary waves is not only of theoretical interest but required to predict the wave run-up on coastal defenses, to assess the impact loads on bridge piers and offshore structures, to design solutions to reduce the effect of resonance in harbors, and to determine the flood risk in river systems. A solitary wave's ability to travel long distances with little loss of energy and shape makes it terrifying and challenging to design against [21]. Nonlinear equations that allow soliton solutions are thus valuable, providing the theoretical tools to design more reliable and safe coastal and hydraulic structures, while also captivating and inspiring the physicist and the mathematician alike [22]. In this sense, the (3+1)-dimensional P-type model offers a more complicated and realistic scenario of the existence of nonlinear waves in higher-dimensional space, where the waves can propagate, interact, diffuse, and converge in different spatial directions, a case that is more similar to the actual situation in many hydro-systems.

In addition, the ability to achieve a detailed and fundamental understanding of the intrinsic dynamics of complex physical systems relies on acquiring exact solutions to the equations that describe the underlying dynamics of various natural and technological systems. The importance of such exact solutions certainly goes beyond their straightforward ability to describe the system dynamics. They provide fundamental bench-marking; stimulate further theoretical inquiries; and frequently represent the essential starting point for the more sophisticated analysis of systems, such as their stability, optimization, and numerical model validation. To obtain such solutions, it is necessary to describe the system's dynamics in the exact language of ordinary or partial differential equations that capture the physical laws, conservation laws, and constitutive laws of the system. For the overwhelming majority of real-world situations involving nonlinear interactions, nonlinear systems have emerged as the preferred and essential tool for the modeling of complex systems that arise in fluid dynamics, plasma physics, optics, geophysics, and hydraulic engineering. The inherent challenges of solving these nonlinear systems—due to the loss of superposition, the emergence of multiple scales, and the possibility of chaotic and solutions—has, over decades, led to the development of a rich and ever expanding suite of analytical, semi-analytical, and symbolic approaches. Over the last few years, a number of these powerful methods have been the subject of intense focus. These include the Adomian decomposition technique [23], the generalized Arnous approach [24], the Lie symmetry method [25], bifurcation analysis [26], the modified Sardar sub-equation technique [27], the Riccati equation mapping approach [28], and the fractional sub-equation neural network technique [29], among others, each with its own strengths for exploring the solution spaces of increasingly complex nonlinear models.

Motivated by the limitations of existing analytical approaches, this study investigates the analytical solutions of the (3+1)-dimensional P-type model using the modified generalized Riccati equation mapping neural network (MGREMNN) method. The main novelty of this work lies in incorporating the modified generalized Riccati equation mapping into a neural-network-based solution framework to construct analytical wave solutions. Specifically, this study aims to derive different families of exact solutions, examine the effectiveness of the proposed method, and identify potential wave structures admitted by the model. By applying the MGREMNN method to a higher-dimensional nonlinear PDE, this work seeks to demonstrate its applicability as an alternative analytical technique for investigating nonlinear wave phenomena. The principal contributions are the construction of

analytical solutions and the assessment of the method's potential and limitations for the considered model.

The remaining part of the paper is organized as follows: Section 2 provides an overview of the neural network model, MGREM-based neural networks, and their graphical representations. Section 3 presents the governing model and application of the technique with the solution's graphical representations. Section 4 presents the concluding comments.

2. Overview of the Modified Generalized Riccati Equation Mapping Approach

$$M\left(u, u_t, u_x, u_y, u_z, u_{tt}, u_{xx}, u_{yy}, u_{zz}, u_t u_x, u_t u_y, u_t u_z \ldots\right) = 0, \tag{1}$$

In this expression, the partial derivatives of $t,\ x,\ y,\ z$ for different unknown functions $u = u(x, y, z, t)$ are described by the notions $u_t,\ u_x,\ u_y,\ u_z, \ldots$.

We will use the MGREM [30] to find the solutions to the ordinary differential equation $\varphi^{'}(x) = \varrho_0 + \varrho_1(x) + \varrho_2(x)^2,\ \ \varrho_2 \neq 0$.

2.1. Neural Network Model

The neural network (NN) architecture is used to construct the trial function, which is then used to calculate the exact solutions of Equation (1). The trial function is used to derive the solutions of Equation (1) from the neural network's output. Next, we may express the trial function of the suggested method as

$$u = \varpi_{l_{nu}} F_{l_i}(\zeta_{l_i}). \tag{2}$$

The weight parameter that connects the final hidden layer l_n to the output layer u is denoted as $\varpi_{l_{nu}}$ in this context, and F represents an activation function in general. For the last hidden layer, the neurons are specified by the set $l_n = \{I_{n-1} + 1, I_{n-1} + 2, \cdots, I_n\}$. The neural network model is affected by parameters such as bias term (b_l) and weights $(\varpi_{i,j})$. The mathematical expression of ζ_{l_i} is given in the l_i-th layer as

$$\zeta_{l_i} = b_{l_i} + \omega_{l_{i-1} l_i} F_{l_{i-1}}\left(\zeta_{l_{i-1}}\right),\ i = 1, 2, \ldots, n,$$

along with

$$l_p = \{x,\ y,\ z, \ldots, t\} (p = 2, 3, \ldots, n-1).$$

The forward propagation technique will be used by neural networks in order to perform their functions more effectively. Additionally, for the process of data transmission between the various layers of this network, it requires multiplication by the weighted sums at each model layer before activation functions may be applied to the input. Thus, the suggested method has the potential to generate new solutions for the model in consideration.Moreover, the detail is given in Figure 1.

2.2. Mgrem Neural Network Approach

The MGREMNN technique is a new approach that combines neural network techniques with the MGREM method. The MGREMNN approach mainly consists of two parts. One important feature is that the activation functions in the first hidden layer can be constructed using solutions obtained from the MGREM approach. Writing these solutions in algebraic form makes it simpler to deal with and understand the PDEs.

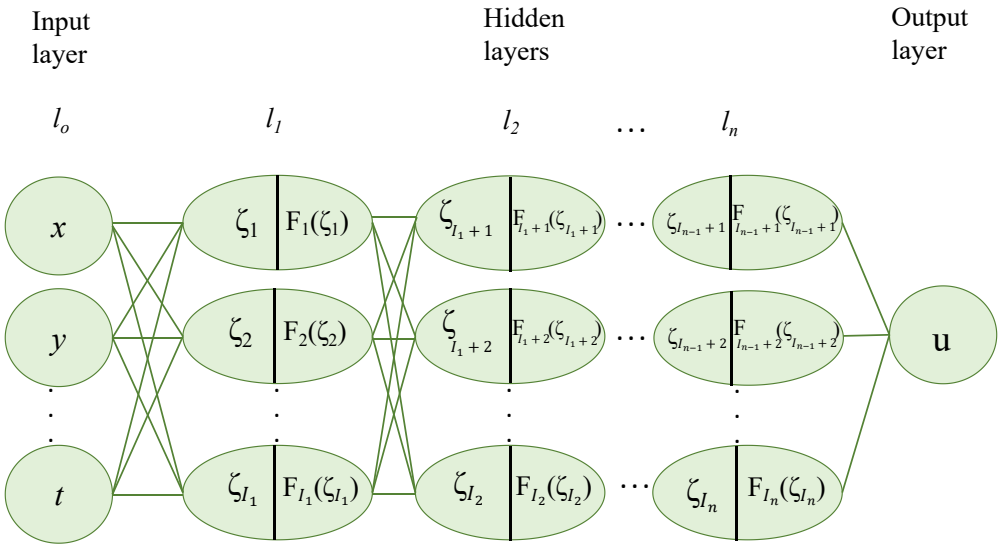


Figure 1. The n-hidden layer neural networking model.

In this framework, the activation functions of the first hidden layer are chosen directly from MGREM solutions by linking the method with neural networks. This connection creates a more flexible structure that can better capture the complex behavior of the equations. As a result, it becomes possible to obtain new exact solutions of PDEs that are not easy to derive using traditional methods. The main components of the proposed approach are given as follows:

Step-1: The Riccati equation may be chosen as the target equation by using the MGREM and the activation functions of the first hidden layer in the NNs model.
Step-2: The MGREMNN architecture may be formed using the activation function of the first hidden layer that was selected in Step 1. This model, which utilizes x, y, z and t as input variables, can figure out how to set up the next hidden layer based on the context. The required results of this can be obtained with the feed-forward process. The NN model details for this procedure are given in Figure 2.
Step-3: Based on the forward propagation of the MGREMNN framework, it is possible to derive the trial functions linked to the solutions of PDEs.
Step-4: We can acquire the algebraic equations by employing the MGREMNN technique trial functions and the PDEs that are associated with these functions.
Step-5: We solve algebraic equations with variables such as x, y, ,z, t, and the corresponding function $F(x, y, z, t), \cdots$. Following that, we write down the expressions in Step 4, and we may make a system of algebraic equations by making the coefficient of each term equal to zero.
Step-6: We examine every potential solution with the algebraic equations for calculating the coefficients and determine the most suitable one that meets the requirements. One way to get the first explicit solutions of u is to input these values back into the trial function.

By allocating a sufficient number of neurones, which are MGREM solutions, to the first hidden layer of the NNs development, this approach accomplishes its aim of discovering exact solutions, which is an obvious advantage.

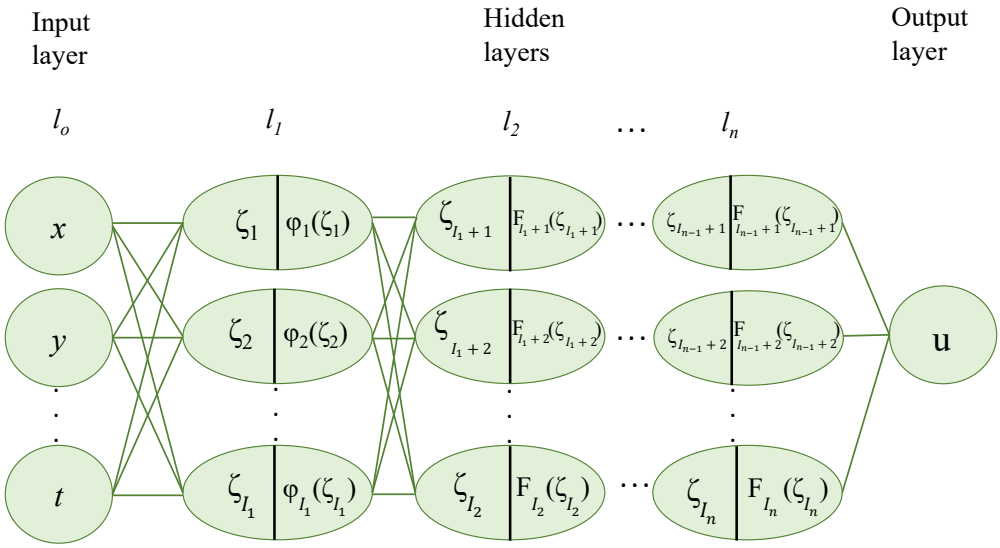


Figure 2. The n-hidden layer MGREM approach neural networking model.

3. The (3+1)-Dimensional Model P-Type Model

In ocean and hydraulic engineering, higher-order nonlinear equations like the P-type (3+1)-dimensional equation are essential for modeling complex wave processes, such as wave breaking, refraction, and nonlinear interactions in shallow water. This equation enables the engineers to predict the frequency of the waves and energy interactions in coastal areas, which is used in the design of offshore structures and breakwaters. It also helps in the study of currents caused by waves and beach erosion, which is important in the conservation of navigation channels and prevention of coastal erosion. The (3+1)-dimensional model also more realistically describes the spatiotemporal development of waves compared to lower-dimensional models, which is helpful in tsunami risk assessment. In the case of hydraulic structures, the equations will be used to model unsteady flows in reservoirs and spillways to provide effective discharge of floods. Its ability to simulate the wave propagation in both directions helps to analyze the resonance in harbors and eliminate dangerous oscillations. The addition of pressure gradients and dispersion enhances prediction of wave–structure interaction in storm surge barriers. Finally, this model links theoretical nonlinear wave physics with engineering applications for sustainable coastal and hydrologic systems. The mathematical form of the proposed model [31–35] is described by

$$u_{xxxy} + \lambda_1 u_{yt} + \lambda_2 (u u_x)_y + \lambda_3 u_{xx} + \lambda_4 u_{zz} = 0, \tag{3}$$

where $u = u(x, y, z, t)$ represents the wave field. The proposed model is a nonlinear dispersive wave equation that combines transport, nonlinearity, and higher dimention dispersion. The interaction of the model's nonlinear dispersive and steepening effects can prevent the shock formation, where these behaviors of smoothing wave profiles depends on the parameters λ_1, λ_2, λ_3, λ_4. Its term-by-term explanation is given as follows:

- u_{xxxy} represents anisotropic dispersion (wave spreading behaves differently in different directions).
- $\lambda_1 u_{yt}$ describes how the wave evolves in time along the y-direction, where λ_1 controls the strength of temporal evolution or wave speed.
- $\lambda_2 (u u_x)_y$: $u u_x$ represents self-interaction of the wave (steepening effect), and taking $()_y$ spreads this nonlinearity along the y-direction. λ_2 controls the strong nonlinear effects; physically, this term is responsible for wave steepening and soliton formation.
- $\lambda_3 u_{xx}$ represents dispersion or diffusion along the x-direction and helps to balance the nonlinear term, where λ_3 determines how strongly waves spread or smooth out in x.

- $\lambda_4 u_{zz}$: This is a transverse spatial effect in the z-direction, represents variation of the wave in the third spatial dimension, and is important for 3D wave propagation, where λ_4 controls spreading or curvature in the z-direction.

In addition, the presented model is studied in the literature with the application of these different techniques: for example, in [31], different soliton solutions have been calculated with the application of various techniques, namely the generalized Arnous method, F-expansion method, and Kumar Malik method, and in [32], the generalized exponential differential function method is used to study its various solution. Moreover, in [33], bifurcation and chaotic analysis are studied in detail, where different new soliton solutions are studied with the application of the Sardar subequation technique, while the proposed model Painlevé analysis and wave interactions are studied in [34]. In [35], the model's analytical and numerical solutions are investigated with the application of the modified extended tanh-function technique.

Application of the Neural Network Technique

The soliton solutions of the (3+1)-dimensional P-type model are investigated in this section. To solve the problem described by the proposed model, we employ the 4-2-2-1 MGREMNN approach, which consists of four neurons in the input layer, two neurons in each hidden layer, and one neuron in the output (trial function u) layer:

$$u = b_5 + \varpi_{3u} F_3(\zeta_3) + \varpi_{4u} F_4(\zeta_4), \tag{4}$$

where

$$\begin{cases} \zeta_1 = b_1 + t\varpi_{t1} + x\varpi_{x1} + y\varpi_{y1} + z\varpi_{z1}, \\ \zeta_2 = b_2 + t\varpi_{t2} + x\varpi_{x2} + y\varpi_{y2} + z\varpi_{z2}, \\ \zeta_3 = b_3 + \varpi_{13} F_1(\zeta_1) + \varpi_{23} F_2(\zeta_2), \\ \zeta_4 = b_4 + \varpi_{14} F_1(\zeta_1) + \varpi_{24} F_2(\zeta_2). \end{cases} \tag{5}$$

In this context, the activation function is denoted by F_i for $(i = 1, 2, 3, 4)$; the corresponding real values to be identified later on are denoted by b_l for $(l = 1, 2, 3, 4, 5)$ and $\varpi_{j,k}$ for $(j = x, y, z, t, 1, 2, 3, 4,\ k = 1, 2, 3, 4,\ j \neq k)$.

For this model, we use the 4-2-2-1 MGREMNNs model to get the solutions. As a result of the inputs x, y, z and t representing the spatial and temporal variables, respectively, the activation functions of the first hidden layer are defined by the solutions of the Riccati equation $\varphi(\cdot)$, which aids in the more effective capture of nonlinear behaviors. On the other hand, the activation functions of the second layer are the identity function $(\cdot)$ and the square function $(\cdot)^2$. Presented below is the output representation of the NNs, which is used as the trial function for PDEs to approximate the underlying solution of the system:

$$u = b_5 + \varpi_{3u}(\zeta_3) + \varpi_{4u}(\zeta_4), \tag{6}$$

where

$$\begin{cases} \zeta_1 = b_1 + t\varpi_{t1} + x\varpi_{x1} + y\varpi_{y1} + z\varpi_{z1}, \\ \zeta_2 = b_2 + t\varpi_{t2} + x\varpi_{x2} + y\varpi_{y2} + z\varpi_{z2}, \\ \zeta_3 = b_3 + \varpi_{13}\varphi(\zeta_1) + \varpi_{23}\varphi(\zeta_2), \\ \zeta_4 = b_4 + \varpi_{14}\varphi(\zeta_1) + \varpi_{24}\varphi(\zeta_2). \end{cases} \tag{7}$$

Figure 3 provides a straightforward and easy-to-understand representation of the 4-2-2-1 MGREMNNs model's structure. We set $b_5 = b$ in the actual implementation, but for $i = 1, 2, 3, 4$, we take $b_i = 0$ for computational simplicity and to eliminate unneeded complexity in the computations. Given these parameters, the 4-2-2-1 MGREMNN model's formula appears as follows:

$$\begin{aligned} u =& b + \varpi_{3u}\left(\varpi_{13}\varphi\left(t\varpi_{t1} + x\varpi_{x1} + y\varpi_{y1} + z\varpi_{z1}\right) + \varpi_{23}\varphi\left(t\varpi_{t2} + x\varpi_{x2} + y\varpi_{y2} + z\varpi_{z2}\right)\right) \\ &+ \varpi_{4u}\left(\varpi_{14}\varphi\left(t\varpi_{t1} + x\varpi_{x1} + y\varpi_{y1} + z\varpi_{z1}\right) + \varpi_{24}\varphi\left(t\varpi_{t2} + x\varpi_{x2} + y\varpi_{y2} + z\varpi_{z2}\right)\right)^2. \end{aligned} \tag{8}$$

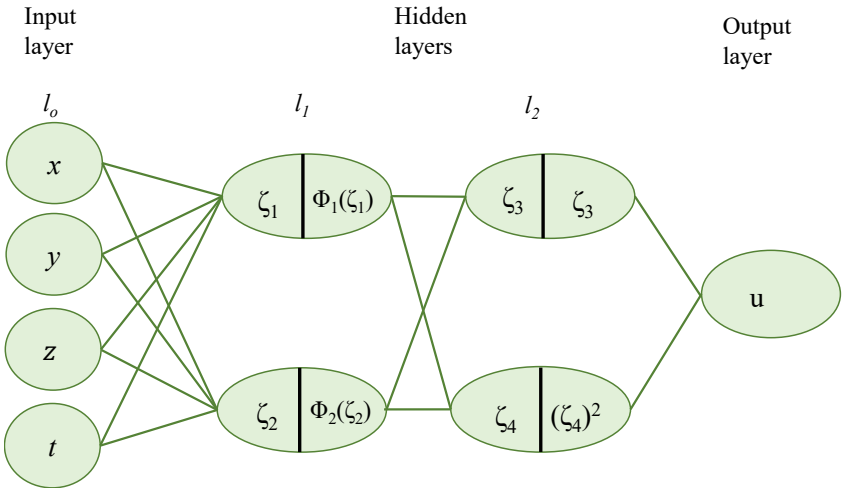


Figure 3. 4–2–2–1 MGREMNN model of Equation (6).

Next, for calculating the solutions, substituting Equation (8) into Equation (3), and simplifying the results, we obtain the solutions as follows:

(I) When $\Omega = \varrho_1^2 - 4\varrho_0\varrho_2 > 0$, $\varrho_1\varrho_2 \neq 0$, $\varrho_0\varrho_2 \neq 0$ and $\varpi_{14} = 0$, $\varpi_{y2} = 0$, $\varpi_{x1} = 0$, $\varpi_{z2} = \frac{\sqrt{-\lambda_3}\varpi_{x2}}{\sqrt{\lambda_4}}$, and $\varpi_{3u} = 0, \lambda_2 = --\frac{2\varrho_2^2\varpi_{x2}^2}{\varpi_{24}^2\varpi_{4u}}$, the solutions can be obtained as follows:

The kink-type soliton solution:

$$u_1(x,y,z,t) = b + \frac{\varpi_{24}^2\varpi_{4u}\left(\sqrt{\Omega}\tanh\left(\frac{1}{2}\sqrt{\Omega}\left(t\varpi_{t2} + x\varpi_{x2} + \frac{\sqrt{-\lambda_3}z\varpi_{x2}}{\sqrt{\lambda_4}}\right)\right) + \varrho_1\right)^2}{4\varrho_2^2}. \tag{9}$$

The explicit solitary wave solution:

$$u_2(x,y,z,t) = b + \frac{\varpi_{24}^2\varpi_{4u}\left(\sqrt{\Omega}\coth\left(\frac{1}{2}\sqrt{\Omega}\left(t\varpi_{t2} + x\varpi_{x2} + \frac{\sqrt{-\lambda_3}z\varpi_{x2}}{\sqrt{\lambda_4}}\right)\right) + \varrho_1\right)^2}{4\varrho_2^2}. \tag{10}$$

The combined bright-dark soliton solution:

$$u_3(x,y,z,t) = b + \frac{\varpi_{24}^2\varpi_{4u}\left(\varrho_1 + \sqrt{\Omega}\left(\tanh\left(\Omega\left(t\varpi_{t2} + x\varpi_{x2} + \frac{\sqrt{-\lambda_3}z\varpi_{x2}}{\sqrt{\lambda_4}}\right)\right) + i\,\mathrm{sech}\left(\sqrt{\Omega}\left(t\varpi_{t2} + x\varpi_{x2} + \frac{\sqrt{-\lambda_3}z\varpi_{x2}}{\sqrt{\lambda_4}}\right)\right)\right)\right)^2}{4\varrho_2^2}. \tag{11}$$

The explicit solitary wave solution:

$$u_4(x,y,z,t) = b + \frac{\varpi_{24}^2\varpi_{4u}\left(\sqrt{\Omega}\left(\coth\left(\sqrt{\Omega}\left(t\varpi_{t2} + x\varpi_{x2} + \frac{\sqrt{-\lambda_3}z\varpi_{x2}}{\sqrt{\lambda_4}}\right)\right) + \mathrm{csch}\left(\sqrt{\Omega}\left(t\varpi_{t2} + x\varpi_{x2} + \frac{\sqrt{-\lambda_3}z\varpi_{x2}}{\sqrt{\lambda_4}}\right)\right)\right) + \varrho_1\right)^2}{4\varrho_2^2}. \tag{12}$$

When $\Omega = \varrho_1^2 - 4\varrho_0\varrho_2 > 0$, $\varrho_1\varrho_2 \neq 0$, $\varrho_0\varrho_2 \neq 0$ and $\varpi_{24} = 0$, $\varpi_{x2} = 0$, $\varpi_{y2} = 0$, $\varpi_{y1} = 0$, $\varpi_{z1} = -\frac{\sqrt{-\lambda_3}\varpi_{x1}}{\sqrt{\lambda_4}}$, $\varpi_{z2} = 0$, $\varpi_{3u} = \frac{\varpi_{14}^2\varrho_1\varpi_{4u}}{\varpi_{13}\varrho_2}$, and $\lambda_2 = -\frac{12\varrho_2^2\varpi_{x1}^2}{\varpi_{14}^2\varpi_{4u}}$, we have the following solutions:

$$\begin{aligned} u_5(x,y,z,t) = {} & \frac{1}{4\varpi_{13}\varrho_2^2}\times \\ & \left(\varpi_{13}\left(4b\varrho_2^2 + \varpi_{14}^2\varpi_{4u}\left((\varrho_1^2 - 4\varrho_0\varrho_2)\operatorname{csch}^2\left(\frac{\Gamma\sqrt{\Omega}}{2}\right) - 4\varrho_0\varrho_2\right)\right) + \right. \\ & \left.\varpi_{14}^2\varpi_{23}\varrho_1\varpi_{4u}\left(-\sqrt{\Omega}\tanh\left(\frac{1}{4}t\sqrt{\Omega}\varpi_{t2}\right)\left(\coth^2\left(\frac{1}{4}t\sqrt{\Omega}\varpi_{t2}\right) + 1\right) - 2\varrho_1\right)\right), \end{aligned} \tag{13}$$

$$\begin{aligned} u_6(x,y,z,t) = {} & b + \frac{\varpi_{14}^2\varpi_{4u}\left(\frac{c\sqrt{\Omega}\cosh\left(\Gamma\sqrt{\Omega}\right) - \sqrt{\Omega(c^2+d^2)}}{c\sinh\left(\Gamma\sqrt{\Omega}\right)+d} + \varrho_1\right)^2}{4\varrho_2^2} \\ & + \frac{\varpi_{14}^2\varrho_1\varpi_{4u}\left(\varpi_{13}\left(\frac{\sqrt{\Omega(c^2+d^2)} - c\sqrt{\Omega}\cosh\left(\Gamma\sqrt{\Omega}\right)}{c\sinh\left(\Gamma\sqrt{\Omega}\right)+d} - \varrho_1\right) + \varpi_{23}\left(\frac{\sqrt{\Omega(c^2+d^2)} - c\sqrt{\Omega}\cosh\left(t\sqrt{\Omega}\varpi_{t2}\right)}{c\sinh\left(t\sqrt{\Omega}\varpi_{t2}\right)+d} - \varrho_1\right)\right)}{2\varpi_{13}\varrho_2^2}, \end{aligned} \tag{14}$$

$$\begin{aligned} u_7(x,y,z,t) = {} & b + \frac{\varpi_{14}^2\varpi_{4u}\left(\frac{\sqrt{\Omega(c^2+d^2)} + c\sqrt{\Omega}\cosh\left(\Gamma\sqrt{\Omega}\right)}{c\sinh\left(\Gamma\sqrt{\Omega}\right)+d} + \varrho_1\right)^2}{4\varrho_2^2} \\ & + \frac{\varpi_{14}^2\varrho_1\varpi_{4u}\left(\varpi_{13}\left(-\frac{\sqrt{\Omega(c^2+d^2)} + c\sqrt{\Omega}\cosh\left(\Gamma\sqrt{\Omega}\right)}{c\sinh\left(\Gamma\sqrt{\Omega}\right)+d} - \varrho_1\right) + \varpi_{23}\left(-\frac{\sqrt{\Omega(c^2+d^2)} + c\sqrt{\Omega}\cosh\left(t\sqrt{\Omega}\varpi_{t2}\right)}{c\sinh\left(t\sqrt{\Omega}\varpi_{t2}\right)+d} - \varrho_1\right)\right)}{2\varpi_{13}\varrho_2^2}, \end{aligned} \tag{15}$$

where $\Gamma = t\varpi_{t1} + \varpi_{x1}\left(x - \frac{\sqrt{-\lambda_3}z}{\sqrt{\lambda_4}}\right)$.

When $\Omega = \varrho_1^2 - 4\varrho_0\varrho_2 > 0$, $\varrho_1\varrho_2 \neq 0$, $\varrho_0\varrho_2 \neq 0$ and $\varpi_{y2} = 0, \varpi_{y1} = 0$, $\varpi_{z1} = \frac{\sqrt{-\lambda_3}\varpi_{x1}}{\sqrt{\lambda_4}}$, and $\varpi_{z2} = \frac{\sqrt{-\lambda_3}\varpi_{x2}}{\sqrt{\lambda_4}}$, we get the following solitary wave solutions:

$$\begin{aligned} u_8(x,y,z,t) = {} & b + 2\varrho_0\varpi_{3u}\left(\frac{\varpi_{13}\cosh\left(\frac{\Gamma\sqrt{\Omega}}{2}\right)}{\sqrt{\Omega}\sinh\left(\frac{\Gamma\sqrt{\Omega}}{2}\right) - \varrho_1\cosh\left(\frac{\Gamma\sqrt{\Omega}}{2}\right)} + \frac{\varpi_{23}\cosh\left(\frac{\Psi\sqrt{\Omega}}{2}\right)}{\sqrt{\Omega}\sinh\left(\frac{\Psi\sqrt{\Omega}}{2}\right) - \varrho_1\cosh\left(\Psi\sqrt{\Omega}\right)}\right) \\ & + 4\varrho_0^2\varpi_{4u}\left(\frac{\varpi_{14}\cosh\left(\frac{\Gamma\sqrt{\Omega}}{2}\right)}{\sqrt{\Omega}\sinh\left(\frac{\Gamma\sqrt{\Omega}}{2}\right) - \varrho_1\cosh\left(\frac{\Gamma\sqrt{\Omega}}{2}\right)} + \frac{\varpi_{24}\cosh\left(\frac{\Psi\sqrt{\Omega}}{2}\right)}{\sqrt{\Omega}\sinh\left(\frac{\Psi\sqrt{\Omega}}{2}\right) - \varrho_1\cosh\left(\frac{\Psi\sqrt{\Omega}}{2}\right)}\right)^2, \end{aligned} \tag{16}$$

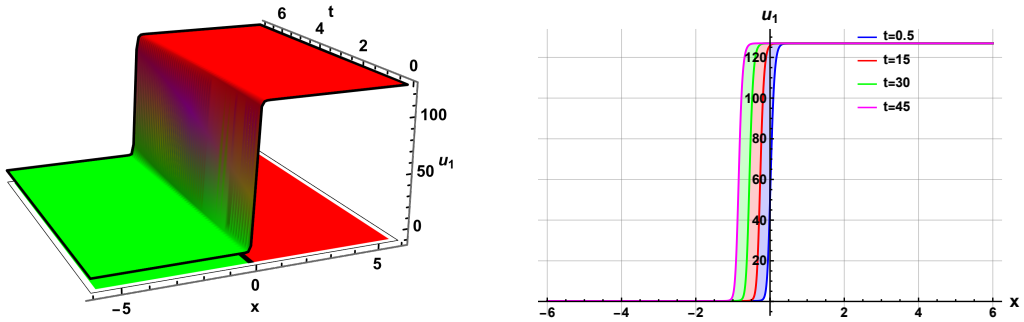
$$\begin{aligned} u_9(x,y,z,t) = {} & b + \\ & 2\varrho_0\varpi_{3u}\left(-\frac{\varpi_{13}\cosh\left(\Gamma\sqrt{\Omega}\right)}{\varrho_1\cosh\left(\Gamma\sqrt{\Omega}\right) - \sqrt{\Omega}\left(\sinh\left(\Gamma\sqrt{\Omega}\right) + i\right)} - \frac{\varpi_{23}\cosh\left(\Psi\sqrt{\Omega}\right)}{\varrho_1\cosh\left(\Psi\sqrt{\Omega}\right) - \sqrt{\Omega}\left(\sinh\left(\Psi\sqrt{\Omega}\right) + i\right)}\right) \\ & + 4\varrho_0^2\varpi_{4u}\left(\frac{\varpi_{14}\cosh\left(\Gamma\sqrt{\Omega}\right)}{\varrho_1\cosh\left(\Gamma\sqrt{\Omega}\right) - \sqrt{\Omega}\left(\sinh\left(\Gamma\sqrt{\Omega}\right) + i\right)} + \frac{\varpi_{24}\cosh\left(\Psi\sqrt{\Omega}\right)}{\varrho_1\cosh\left(\Psi\sqrt{\Omega}\right) - \sqrt{\Omega}\left(\sinh\left(\Psi\sqrt{\Omega}\right) + i\right)}\right)^2, \end{aligned} \tag{17}$$

$$\begin{aligned} u_{10}(x,y,z,t) = {} & b + \\ & 2\varrho_0\varpi_{3u}\left(-\frac{\varpi_{13}\sinh\left(\Gamma\sqrt{\Omega}\right)}{\varrho_1\sinh\left(\Gamma\sqrt{\Omega}\right) - \sqrt{\Omega}\left(\cosh\left(\Gamma\sqrt{\Omega}\right) + 1\right)} - \frac{\varpi_{23}\sinh\left(\Psi\sqrt{\Omega}\right)}{\varrho_1\sinh\left(\Psi\sqrt{\Omega}\right) - \sqrt{\Omega}\left(\cosh\left(\Psi\sqrt{\Omega}\right) + 1\right)}\right) \\ & + 4\varrho_0^2\varpi_{4u}\left(\frac{\varpi_{14}\sinh\left(\Gamma\sqrt{\Omega}\right)}{\varrho_1\sinh\left(\Gamma\sqrt{\Omega}\right) - \sqrt{\Omega}\left(\cosh\left(\Gamma\sqrt{\Omega}\right) + 1\right)} + \frac{\varpi_{24}\sinh\left(\Psi\sqrt{\Omega}\right)}{\varrho_1\sinh\left(\Psi\sqrt{\Omega}\right) - \sqrt{\Omega}\left(\cosh\left(\Psi\sqrt{\Omega}\right) + 1\right)}\right)^2, \end{aligned} \tag{18}$$

where $\Gamma = t\varpi_{t1} + \varpi_{x1}\left(x + \frac{\sqrt{-\lambda_3}z}{\sqrt{\lambda_4}}\right)$, $\Psi = t\varpi_{t2} + \varpi_{x2}\left(x + \frac{\sqrt{-\lambda_3}z}{\sqrt{\lambda_4}}\right)$.

- **Graphical interpretation of the obtained solutions with application in ocean and hydraulic engineering**

Three-dimensional (3D), two-dimensional (2D), and contour plots are essential and complementary tools in ocean and hydraulic engineering to convert large data sets into meaningful physical understanding. A well-crafted three-dimensional surface plot offers an immediate, intuitive perception of the general form and extent of a process such as the progression of a tsunami wave traveling over a basin or the distribution of force on the face of a dam, enabling engineers to quickly understand spatial relationships, as well as maximum and minimum values. Using this bird's eye view, the analyses are refined by 2D profile plots, which are essential for extracting quantitative information along specific lines, such as the cross-shore profile of velocity or the elevation profile of water surface along the center line of a channel, allowing for verification with analytical formulas and laboratory data. Lastly, contour graphs move a qualitative interpretation of the problem to quantitative design issues by overlaying contours of equal value (e.g., bathymetry, wave height, or scour potential) onto a plan view. This is possibly the most appropriate form of representation to engineering design as it allows the instantaneous definition of the flood zones, optimal location of breakwaters to circumvent areas of high wave energy, and essential velocity profiles that control the transportation and stability of the sediment. The figures of the extracted solutions with applications are discussed as follows: The kink-type dynamics of the solution (9) is represented in Figure 4 with the assistance of the parametric values $b = 0.0091$, $\lambda_3 = -0.002$, $\lambda_4 = 0.32$, $z = 0.2$, $\varpi_{24} = 1.47$, $\varrho_1 = 1.6$, $\varrho_0 = 0.2$, $\varrho_2 = 0.5$, $\varpi_{t2} = 0.232$, $\varpi_{4u} = 6.234$, and $\varpi_{x2} = 12$.



(**a**) (**b**)

Figure 4. Plots to the solution (9). (**a**) Three-dimensional and contour plots. (**b**) Two-dimensional plot.

Simple mathematical models of propagating shallow-water fronts include kink-shaped solutions, where a smooth kink between two constant states is used. Their graphs are crucial to depict the abrupt, stable change in water surface level across a hydraulic jump, connecting subcritical and supercritical flow states. In tides, kink-type waves (undular bores) model the sudden elevation change in bore propagation, enabling engineers to forecast run-up and warning levels. The kink profile also represents the interface of fluids with different densities (e.g., salt and fresh water in estuaries), which is essential for navigation channel siltation and intake designs. Their inherent stability offers a diagnostic criterion; if a numerical model fails to preserve a kink profile in a dam-break front simulation, it indicates numerical diffusion and requires mesh refinement. The graph of the kink's width and steepness yields the turbulent eddy viscosity coefficient, linking the field observations to the energy dissipation.

Moreover, the absolute (a, b), real (c, d), and imaginary (e, f) dynamics are shown in Figure 5 for the solution (11) with the parametric values $b = 1$, $\lambda_3 = -0.002$, $\lambda_4 = 0.32$, $z = 2.89$, $\varpi_{24} = 0.47$, $\varrho_1 = 5.6$, $\varrho_0 = 0.2$, $\varrho_2 = 0.5$, $\varpi_{t2} = 0.02$, $\varpi_{4u} = 0.234$, and $\varpi_{x2} = 0.26$.

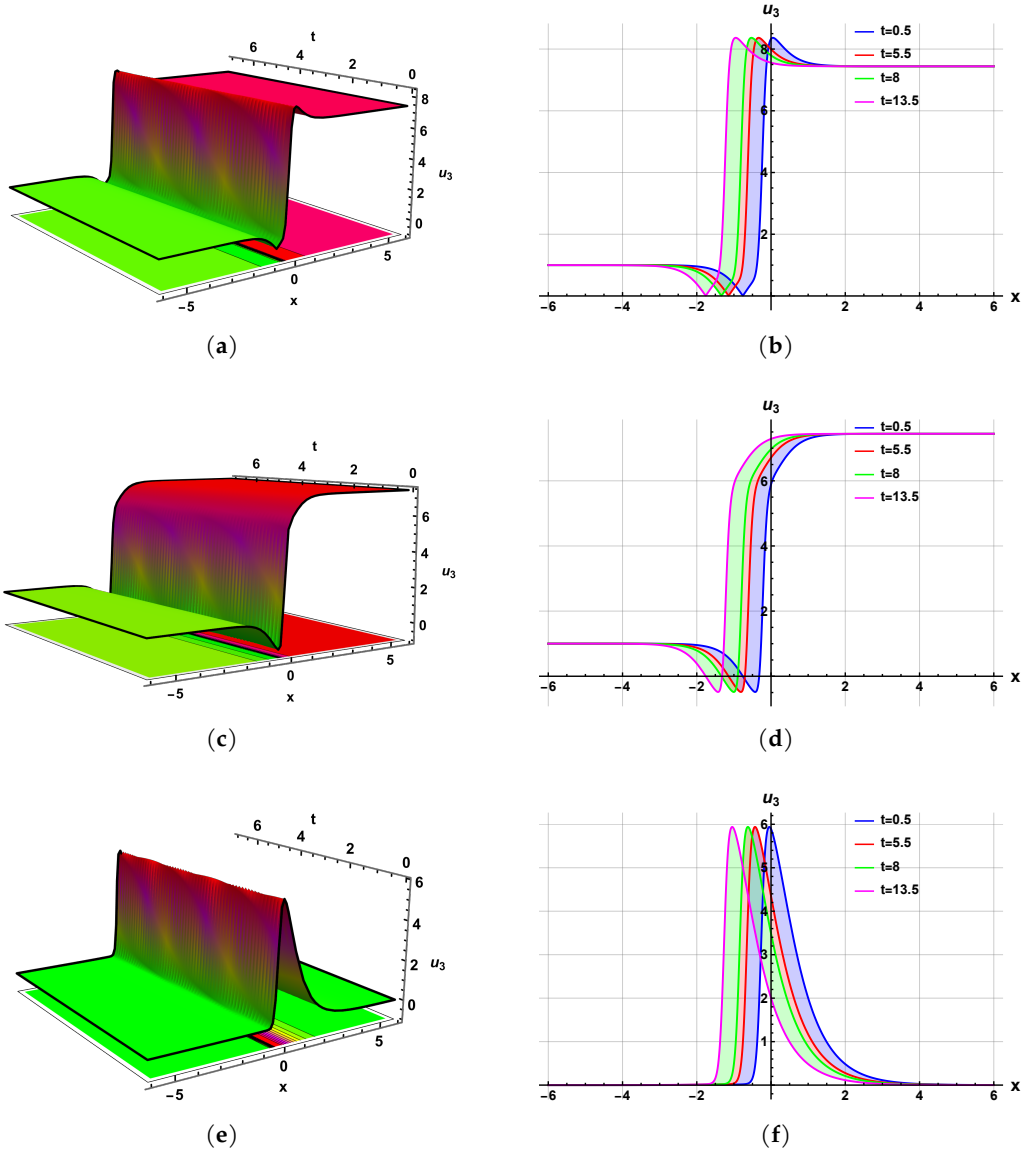
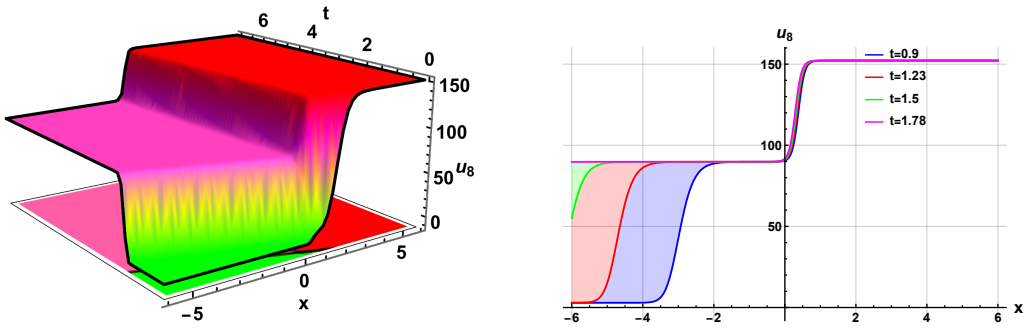


Figure 5. Plots to the solution (11). (**a**) Three-dimensional and contour plots. (**b**) Two-dimensional plot. (**c**) Three-dimensional and contour plots. (**d**) Two-dimensional plot. (**e**) Three-dimensional and contour plots. (**f**) Two-dimensional plot.

Figure 5 shows the dynamics of the combined, dark, and bright solitons. Bright and dark solitons are two prototype examples of stable, coherent, and localized nonlinear wave packets that propagate without distortion, and their graphs are instrumental in understanding different physical phenomena in water. The graph of a bright soliton, which represents a localized elevation from the mean water surface, models both rogue waves in the ocean and tsunami wave trains, allowing engineers to forecast the instantaneous crest of the wave and the impulsive force on offshore structures. A dark soliton, on the other hand, graphically models the propagation of a stable low trough in a shallow-water wave train on a river and represents a localized depression or hole in the water level. The coupled bright-dark soliton, graphically shown as a combined elevation–depression structure, maps onto breather-like structures and modulationally unstable wave groups in crossing seas, a ship, and mooring risk scenario. The soliton graphs enable ocean engineers to estimate the amplitude, width, and propagation speed of a soliton from time series in the field, which are used in basin tests to validate the robustness of coastal structures against focused wave attack. In the context of hydraulics, the trough structure of a dark soliton verifies theoretical

envelope solutions of the studied equation against laboratory data in long wave flumes, a crucial benchmark for numerical wave models to be employed in riverine and estuarine flood routing.

Figure 6 is sketched for the solution (16) for the parametric values $b = 2.91, \lambda_3 = -0.002, \lambda_4 = 0.32, z = 2, \varpi_{13} = 0.4, \varpi_{23} = 1.56, \varpi_{14} = 2.9, \varpi_{24} = 0.9, \varrho_1 = 3.6, \varrho_0 = 0.02, \varrho_2 = 0.5, \varpi_{t1} = 6.232, \varpi_{t2} = 0.33, \varpi_{3u} = 0.07, \varpi_{4u} = 0.2, \varpi_{x1} = 1.2, \varpi_{x2} = 3.2$.



(**a**) (**b**)

Figure 6. Plots to the solution (16). (**a**) Three-dimensional and contour plots. (**b**) Two-dimensional plot.

The 3D solitary wave graph is a comprehensive representation of the whole spatiotemporal evolution of the localized water surface elevation, one axis being distance of propagation and the other axis being time. The surface is a smooth, isolated hump, sharply elevated from a flat plane, and clearly indicates the solitary wave's concentration of energy in a single pulse. The uniform translation of this hump along the distance–time plane reveals that the hump crest height never changes, confirming that there is no dispersion or dissipation of the wave. The solitary wave 2D graphs are obtained from the 3D surface by taking a vertical profile at a given time, each showing a narrow, localized peak of elevation, which remains of the same height and width as it moves.

The real (a, b) and imaginary (c, d) dynamical behaviors are shown in Figure 7 to the solution 17 for the parametric values $b = 0.91, \lambda_3 = -0.2, \lambda_4 = 0.32, z = 0.22, \varpi_{13} = 1.4, \varpi_{23} = 0.56, \varpi_{14} = 0.9, \varpi_{24} = 0.9, \varrho_1 = 0.61, \varrho_0 = 0.02, \varrho_2 = 0.05, \varpi_{t1} = 3.232, \varpi_{t2} = 0.33, \varpi_{3u} = 0.7, \varpi_{4u} = 2.2, \varpi_{x1} = 0.005$, and $\varpi_{x2} = 3.2$.

This figure shows the lump wave dynamics. Lump waves are two-dimensional, algebraically decaying, nonlinear waves that are rationally localized in space. They are a better representation of isolated extreme events than line solitons. Their 3D graphs, which look like a sharply peaked isolated surface mound of water rising from an otherwise flat sea, are necessary to illustrate the fully localized nature of extreme or rogue waves in the ocean. Lump wave contour plots show closed circular rings of fixed height that very accurately define the horizontal spread of high-energy water, allowing engineers to measure impact areas on offshore structures and vessel hulls. In contrast to line solitons, 2D lump wave cross-sections reveal that it has algebraic, not exponential decay, an essential graph that provides a warning of the wider region of wave influence surrounding the lump peak. In water engineering, lump wave graphs verify high-precision numerical modeling of experiments in wave basins where a plunging breaker or focused wave packet creates a three-dimensionally trapped water column that can deliver devastating point impacts.

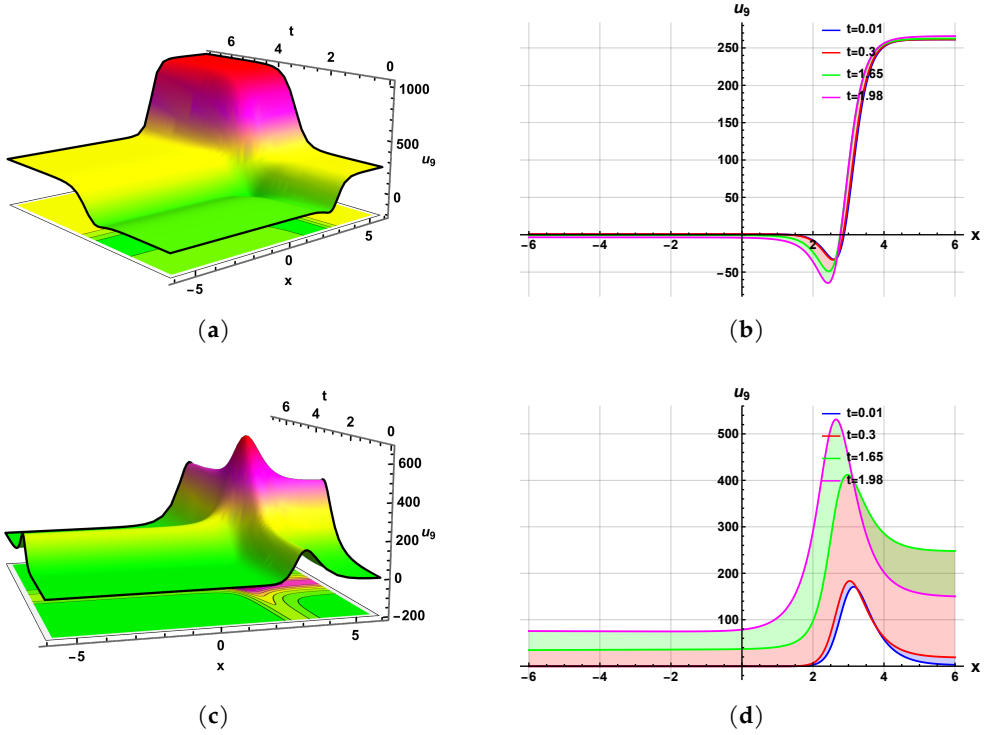


Figure 7. Plots to the solution (17). (**a**) Three-dimensional and contour plots. (**b**) Two-dimensional plot. (**c**) Three-dimensional and contour plots. (**d**) Two-dimensional plot.

(II) When $\Omega = \varrho_1^2 - 4\varrho_0\varrho_2 < 0$, $\varrho_1\varrho_2 \neq 0$, $\varrho_0\varrho_2 \neq 0$ and $\varpi_{y2} = 0$, $\varpi_{y1} = 0$, $\varpi_{z1} = \frac{\sqrt{-\lambda_3}\varpi_{x1}}{\sqrt{\lambda_4}}$, and $\varpi_{z2} = \frac{\sqrt{-\lambda_3}\varpi_{x2}}{\sqrt{\lambda_4}}$, we get the periodic wave solutions

$$u_{11}(x,y,z,t) = b - \frac{\varpi_{3u}\left(\varpi_{13}\left(\varrho_1 - \sqrt{-\Omega}\tan\left(\frac{\Gamma\sqrt{-\Omega}}{2}\right)\right) + \varpi_{23}\left(\varrho_1 - \sqrt{-\Omega}\tan\left(\frac{\Psi\sqrt{-\Omega}}{2}\right)\right)\right)}{2\varrho_2} + \frac{\varpi_{4u}\left(\varpi_{14}\left(\varrho_1 - \sqrt{-\Omega}\tan\left(\frac{\Gamma\sqrt{-\Omega}}{2}\right)\right) + \varpi_{24}\left(\varrho_1 - \sqrt{-\Omega}\tan\left(\frac{\Psi\sqrt{-\Omega}}{2}\right)\right)\right)^2}{4\varrho_2^2}, \tag{19}$$

$$u_{12}(x,y,z,t) = b - \frac{\varpi_{3u}\left(\varpi_{13}\left(\sqrt{-\Omega}\cot\left(\frac{\Gamma\sqrt{-\Omega}}{2}\right) + \varrho_1\right) + \varpi_{23}\left(\sqrt{-\Omega}\cot\left(\frac{\Psi\sqrt{-\Omega}}{2}\right) + \varrho_1\right)\right)}{2\varrho_2} + \frac{\varpi_{4u}\left(\varpi_{14}\left(\sqrt{-\Omega}\cot\left(\frac{\Gamma\sqrt{-\Omega}}{2}\right) + \varrho_1\right) + \varpi_{24}\left(\sqrt{-\Omega}\cot\left(\frac{\Psi\sqrt{-\Omega}}{2}\right) + \varrho_1\right)\right)^2}{4\varrho_2^2}, \tag{20}$$

$$u_{13}(x,y,z,t) = b - \frac{\varpi_{3u}}{2\varrho_2}\left(\varpi_{13}\left(\varrho_1 - \sqrt{-\Omega}\left(\tan\left(\Gamma\sqrt{-\Omega}\right) + \sec\left(\Gamma\sqrt{-\Omega}\right)\right)\right) + \varpi_{23}\left(\varrho_1 - \sqrt{-\Omega}\left(\tan\left(\Psi\sqrt{-\Omega}\right) + \sec\left(\Psi\sqrt{-\Omega}\right)\right)\right)\right) + \frac{1}{4\varrho_2^2}\varpi_{4u}\left(\varpi_{14}\left(\varrho_1 - \sqrt{-\Omega}\left(\tan\left(\Gamma\sqrt{-\Omega}\right) + \sec\left(\Gamma\sqrt{-\Omega}\right)\right)\right) + \varpi_{24}\left(\varrho_1 - \sqrt{-\Omega}\left(\tan\left(\Psi\sqrt{-\Omega}\right) + \sec\left(\Psi\sqrt{-\Omega}\right)\right)\right)\right)^2, \tag{21}$$

$$u_{14}(x,y,z,t) == b - \frac{\varpi_{3u}\left(\varpi_{13}\left(\sqrt{-\Omega}\cot\left(\frac{\Gamma\sqrt{-\Omega}}{2}\right) + \varrho_1\right) + \varpi_{23}\left(\sqrt{-\Omega}\cot\left(\frac{\Psi\sqrt{-\Omega}}{2}\right) + \varrho_1\right)\right)}{2\varrho_2} + \frac{\varpi_{4u}\left(\varpi_{14}\left(\sqrt{-\Omega}\cot\left(\frac{\Gamma\sqrt{-\Omega}}{2}\right) + \varrho_1\right) + \varpi_{24}\left(\sqrt{-\Omega}\cot\left(\frac{\Psi\sqrt{-\Omega}}{2}\right) + \varrho_1\right)\right)^2}{4\varrho_2^2}, \tag{22}$$

where $\Gamma = t\varpi_{t1} + \varpi_{x1}\left(x - \frac{\sqrt{-\lambda_3}z}{\sqrt{\lambda_4}}\right), \Psi = t\varpi_{t2} + \varpi_{x2}\left(x + \frac{\sqrt{-\lambda_3}z}{\sqrt{\lambda_4}}\right)$.

When $\Omega = \varrho_1^2 - 4\varrho_0\varrho_2 < 0$, $\varrho_1\varrho_2 \neq 0$, $\varrho_0\varrho_2 \neq 0$ and $\varpi_{14} = 0, \varpi_{y2} = 0$, $\varpi_{x1} = 0$, $\varpi_{z2} = \frac{\sqrt{-\lambda_3}\varpi_{x2}}{\sqrt{\lambda_4}}$, and $\varpi_{3u} = 0, \lambda_2 = -\frac{2\varrho_2^2\varpi_{x2}^2}{\varpi_{24}^2\varpi_{4u}}$, resulting in solutions as

$$u_{15}(x,y,z,t) = b + \frac{\varpi_{24}^2\varpi_{4u}\left(\sqrt{-\Omega}\left(\tan\left(\frac{\Psi\sqrt{-\Omega}}{4}\right) - \cot\left(\frac{\Psi\sqrt{-\Omega}}{4}\right)\right) - 2\varrho_1\right)^2}{16\varrho_2^2}, \tag{23}$$

$$u_{16}(x,y,z,t) = b + \frac{\varpi_{24}^2\varpi_{4u}\left(\frac{c\sqrt{-\Omega}\cos\left(\Psi\sqrt{-\Omega}\right) - \sqrt{(-\Omega)(d^2-c^2)}}{c\sin\left(\Psi\sqrt{-\Omega}\right)+d} + \varrho_1\right)^2}{4\varrho_2^2}, \tag{24}$$

$$u_{17}(x,y,z,t) = b + \frac{4\varpi_{24}^2\varrho_0^2\varpi_{4u}\cos^2\left(\frac{\Psi\sqrt{-\Omega}}{2}\right)}{\left(\sqrt{-\Omega}\sin\left(\frac{\Psi\sqrt{-\Omega}}{2}\right) + \varrho_1\cos\left(\frac{\Psi\sqrt{-\Omega}}{2}\right)\right)^2}, \tag{25}$$

$$u_{18}(x,y,z,t) = b + \frac{4\varpi_{24}^2\varrho_0^2\varpi_{4u}\sin^2\left(\frac{\Psi\sqrt{-\Omega}}{2}\right)}{\left(\varrho_1\sin\left(\frac{\Psi\sqrt{-\Omega}}{2}\right) - \sqrt{-\Omega}\cos\left(\frac{\Psi\sqrt{-\Omega}}{2}\right)\right)^2}. \tag{26}$$

When $\Omega = \varrho_1^2 - 4\varrho_0\varrho_2 < 0$, $\varrho_1\varrho_2 \neq 0$, $\varrho_0\varrho_2 \neq 0$ and $\varpi_{24} = 0, \varpi_{x2} = 0, \varpi_{y2} = 0, \varpi_{y1} = 0$, $\varpi_{z1} = -\frac{\sqrt{-\lambda_3}\varpi_{x1}}{\sqrt{\lambda_4}}, \varpi_{z2} = 0, \varpi_{3u} = \frac{\varpi_{14}^2\varrho_1\varpi_{4u}}{\varpi_{13}\varrho_2}$, and $\lambda_2 = -\frac{12\varrho_2^2\varpi_{x1}^2}{\varpi_{14}^2\varpi_{4u}}$, representing the derived periodic solutions as

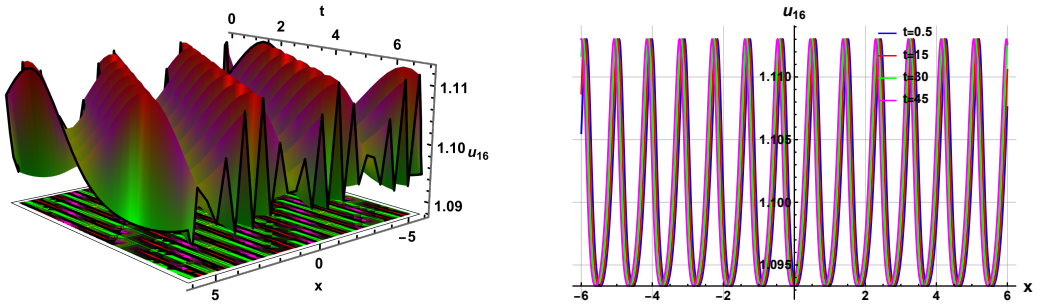
$$\begin{aligned} u_{19}(x,y,z,t) = b &+ \frac{4\varpi_{14}^2\varrho_0^2\varpi_{4u}\cos^2\left(\Gamma\sqrt{-\Omega}\right)}{\left(\sqrt{-\Omega}\left(\sin\left(\Gamma\sqrt{-\Omega}\right)+1\right) + \varrho_1\cos\left(\Gamma\sqrt{-\Omega}\right)\right)^2} \\ &+ \frac{2\varpi_{14}^2\varrho_0\varrho_1\varpi_{4u}\left(-\frac{\varpi_{13}\cos\left(\Gamma\sqrt{-\Omega}\right)}{\sqrt{-\Omega}\left(\sin\left(\Gamma\sqrt{-\Omega}\right)+1\right)+\varrho_1\cos\left(\Gamma\sqrt{-\Omega}\right)} - \frac{\varpi_{23}\cos\left(t\sqrt{-\Omega}\varpi_{t2}\right)}{\sqrt{-\Omega}\left(\sin\left(t\sqrt{-\Omega}\varpi_{t2}\right)+1\right)+\varrho_1\cos\left(t\sqrt{-\Omega}\varpi_{t2}\right)}\right)}{\varpi_{13}\varrho_2}, \end{aligned} \tag{27}$$

$$\begin{aligned} u_{20}(x,y,z,t) = b &+ \frac{4\varpi_{14}^2\varrho_0^2\varpi_{4u}\sin^2\left(\Gamma\sqrt{-\Omega}\right)}{\left(\varrho_1\sin\left(\Gamma\sqrt{-\Omega}\right) - \sqrt{-\Omega}\left(\cos\left(\Gamma\sqrt{-\Omega}\right)+1\right)\right)^2} \\ &\frac{2\varpi_{14}^2\varrho_0\varrho_1\varpi_{4u}\left(-\frac{\varpi_{13}\sin\left(\Gamma\sqrt{-\Omega}\right)}{\varrho_1\sin\left(\Gamma\sqrt{-\Omega}\right)-\sqrt{-\Omega}\left(\cos\left(\Gamma\sqrt{-\Omega}\right)+1\right)} - \frac{\varpi_{23}\sin\left(t\sqrt{-\Omega}\varpi_{t2}\right)}{\varrho_1\sin\left(t\sqrt{-\Omega}\varpi_{t2}\right)-\sqrt{-\Omega}\left(\cos\left(t\sqrt{-\Omega}\varpi_{t2}\right)+1\right)}\right)}{\varpi_{13}\varrho_2}, \end{aligned} \tag{28}$$

where $\Gamma = t\varpi_{t1} + \varpi_{x1}\left(x - \frac{\sqrt{-\lambda_3}z}{\sqrt{\lambda_4}}\right)$.

- **Graphical interpretation of the obtained solutions with application in ocean and hydraulic engineering**

The parameters $b = 1.091$, $c = 1.2, d = 4$, $\lambda_3 = -0.2$, $\lambda_4 = 0.02$, $z = 0.002$, $\varpi_{24} = 0.47$, $\varrho_1 = 0.6$, $\varrho_0 = 1.2$, $\varrho_2 = 2.5$, $\varpi_{t2} = 0.2$, $\varpi_{4u} = 0.1234$, and $\varpi_{x2} = 2$ have been used to observe the periodic dynamics for the solution (24) in Figure 8.

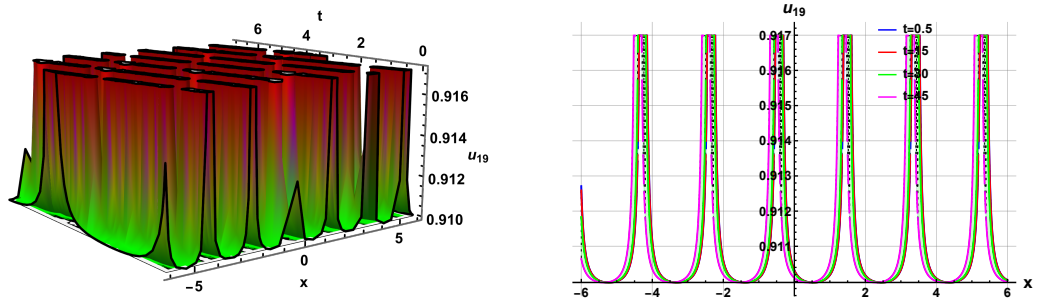


(**a**) (**b**)

Figure 8. Plots to the solution (24). (**a**) Three-dimensional and contour plots. (**b**) Two-dimensional plot.

Periodic wave solutions, which are repetitive in space and time, provide the basic building blocks for describing the majority of real sea states and open-channel flow oscillations of interest to engineers. Their 3-D surface plots, showing continuous, wriggly wave trains that uniformly fill the spatial domain, offer an intuitive grasp of the systematic energy transfer driving swell waves, tidal oscillations, and monochromatic waves in wave flumes. Their corresponding contour maps of periodic waves, showing equally spaced parallel bands of crests and troughs, are vital in delineating regions of constant wave phase and amplitude, and provide the template against which wave diffraction, refraction, and shoaling anomalies are evaluated in coastal engineering.

The periodic behavior of the solution (27) is sketched in Figure 9 for the parametric values $b = 0.91$, $\lambda_3 = -2$, $\lambda_4 = 3.2$, $z = 0.2$, $\varpi_{14} = 0.07$, $\varpi_{13} = 0.7$, $\varpi_{23} = 0.47$, $\varrho_1 = 0.06$, $\varrho_0 = 0.2$, $\varrho_2 = 0.5$, $\varpi_{t1} = 2$, $\varpi_{t2} = 0.2$, $\varpi_{4u} = 0.1234$, and $\varpi_{x1} = 5.2$.



(**a**) (**b**)

Figure 9. Plots to the solution (27). (**a**) Three-dimensional and contour plots. (**b**) Two-dimensional plot.

(III) When $\varpi_{24} = 0$, $\varpi_{x2} = 0$, $\varpi_{y2} = 0$, $\varpi_{y1} = 0$, $\varpi_{z1} = -\frac{\sqrt{-\lambda_3}\varpi_{x1}}{\sqrt{\lambda_4}}$, $\varpi_{z2} = 0$, $\varpi_{3u} = \frac{\varpi_{14}^2\varrho_1\varpi_{4u}}{\varpi_{13}\varrho_2}$, and $\lambda_2 = -\frac{12\varrho_2^2\varpi_{x1}^2}{\varpi_{14}^2\varpi_{4u}}$, with $\varrho_0 = 0$. Consequently, the following are the soliton solutions:

$$u_{21}(x,y,z,t) = b + \frac{\Delta\varpi_{14}^2\varrho_1^2\varpi_{4u}\left(\frac{\sinh(\Gamma\varrho_1)-\cosh(\Gamma\varrho_1)}{(-\sinh(\Gamma\varrho_1)+\cosh(\Gamma\varrho_1)+\Delta)^2} - \frac{\varpi_{23}}{\varpi_{13}(\Delta-\sinh(t\varrho_1\varpi_{t2})+\cosh(t\varrho_1\varpi_{t2}))}\right)}{\varrho_2^2}, \tag{29}$$

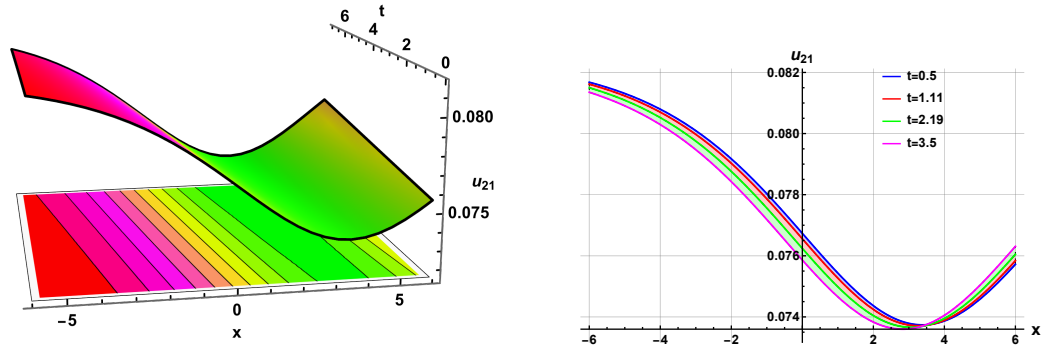
$$\begin{aligned} u_{22}(x,y,z,t) = b &+ \frac{\varpi_{14}^2\varrho_1^2\varpi_{4u}(\cosh(\Gamma\varrho_1)-\sinh(\Gamma\varrho_1))^2}{\varrho_2^2(-\sinh(\Gamma\varrho_1)+\cosh(\Gamma\varrho_1)+\Delta)^2} \\ &+ \frac{\varpi_{14}^2\varrho_1^2\varpi_{4u}\left(\frac{\varpi_{13}(\cosh(\Gamma\varrho_1)-\sinh(\Gamma\varrho_1))}{-\sinh(\Gamma\varrho_1)+\cosh(\Gamma\varrho_1)+\Delta} + \frac{\varpi_{23}(\cosh(t\varrho_1\varpi_{t2})-\sinh(t\varrho_1\varpi_{t2}))}{\Delta-\sinh(t\varrho_1\varpi_{t2})+\cosh(t\varrho_1\varpi_{t2})}\right)}{\varpi_{13}\varrho_2^2}, \end{aligned} \tag{30}$$

$$u_{23}(x,y,z,t) = b + \frac{\varpi_{14}^2\varrho_1^2\varpi_{4u}(\sinh(\Gamma\varrho_1)+\cosh(\Gamma\varrho_1))^2}{\varrho_2^2(\sinh(\Gamma\varrho_1)+\cosh(\Gamma\varrho_1)+\Delta)^2} + \frac{\varpi_{14}^2\varrho_1^2\varpi_{4u}\left(-\frac{\varpi_{13}(\sinh(\Gamma\varrho_1)+\cosh(\Gamma\varrho_1))}{\sinh(\Gamma\varrho_1)+\cosh(\Gamma\varrho_1)+\Delta} - \frac{\varpi_{23}(\sinh(t\varrho_1\varpi_{t2})+\cosh(t\varrho_1\varpi_{t2}))}{\Delta+\sinh(t\varrho_1\varpi_{t2})+\cosh(t\varrho_1\varpi_{t2})}\right)}{\varpi_{13}\varrho_2^2}, \tag{31}$$

where $\Gamma = t\varpi_{t1} + \varpi_{x1}\left(x - \frac{\sqrt{-\lambda_3}z}{\sqrt{\lambda_4}}\right)$.

- **Graphical interpretation of the obtained solutions with application in ocean and hydraulic engineering**

The dynamical behavior of the solution (29) is shown in Figure 10 for the values $b = 0.091$, $\Delta = 0.32$, $\lambda_3 = -5$, $\lambda_4 = 0.2$, $z = 0.12$, $\varpi_{14} = 1.07$, $\varpi_{13} = 3.07$, $\varpi_{23} = 3.07$, $\varrho_1 = 0.06$, $\varrho_2 = 0.5$, $\varpi_{t2} = 0.12$, $\varpi_{t1} = 1.22$, $\varpi_{4u} = 2.1234$, and $\varpi_{x1} = 6.6$.

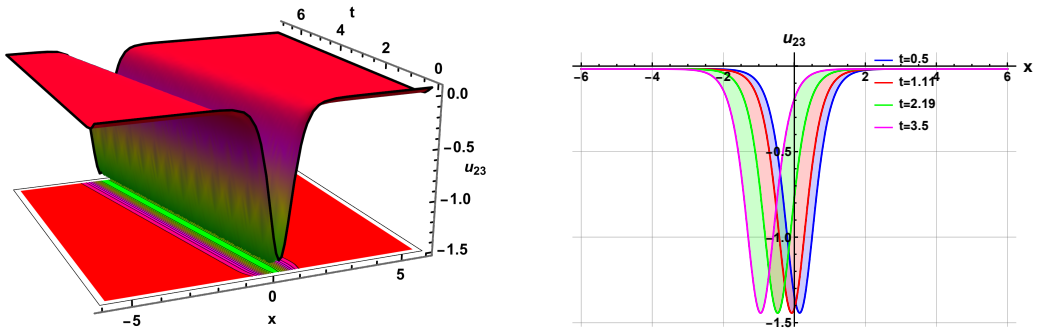


(**a**) (**b**)

Figure 10. Plots to the solution (29). (**a**) Three-dimensional and contour plots. (**b**) Two-dimensional plot.

In the 3D figure, a single, small pulse (with a maximum amplitude of 0.080) is propagating steadily in the x-direction with time, not diffusing. The entire disturbance is contained within this small, non-dispersive hump that keeps its shape as it moves along on a flat background. In water engineering, this type of graph aids in visualizing the passage of a small but sustained water surface disturbance, such as a small flood wave due to partial gate opening or a ship wake, along a channel without spreading, enabling the estimation of its arrival time downstream, and the effects on critical structures such as intake screens or gauging stations. The 2D figure illustrates vertical profile snapshots of the wave component at four different times, each of which exhibits a narrow, steep, pulse-like feature with a slightly different peak amplitude (approximately 0.082) that moves to the right, preserving its confined shape. Moreover, the soliton dynamics has been observed in Figure 11 with the parametric values $b = 0.091$, $\Delta = 3.32$, $\lambda_3 = -0.25$, $\lambda_4 = 1.2$, $z = 0.0.2$, $\varpi_{14} = 1.7$, $\varpi_{13} = 3.7$, $\varpi_{23} = 0.07$, $\varrho_1 = 6$, $\varrho_2 = 1.5$, $\varpi_{t2} = 2.12$, $\varpi_{t1} = 0.22$, $\varpi_{4u} = 0.1234$, and $\varpi_{x1} = 0.6$ to the solution (31).

The 3D graph shows a dark soliton as a stable localized dip or trough that moves at a constant speed along the x-axis as time progresses, with the surface rapidly decreasing from a flat non-zero background to a minimum value and then gradually rising to the background level. In civil and ocean engineering, 3D dark soliton graphs are used to model the movement of stable low-trough states in shallow-water waves and estuarine flows and provide engineers with information on the location and duration of low wave troughs that can expose submerged water intakes or compromise vessel under-keel clearance. The 2D figure shows the vertical profiles of the component at four times, each exhibiting a persistent localized depression that falls from a constant background level (close to zero) to a level of roughly −1.5 and then relaxes back to the background.



(**a**) (**b**)

Figure 11. Plots to the solution (31). (**a**) Three-dimensional and contour plots. (**b**) Two-dimensional plot.

4. Concluding Remarks

To conclude, this paper has presented a novel approach known as the MGREMNN method that elegantly combines the MGREM technique with a neural network to obtain analytical solutions. The new method exhibits impressive efficiency in directly solving the (3+1)-dimensional P-type model, which is a fundamental model of nonlinear wave theory in fluid and plasma physics and is relevant to shallow water waves and hydraulic engineering. Unlike conventional methods, which necessitate awkward transformations, balancing, and iterative reductions to ordinary differential equations, we work directly with the original equation. By using the solutions of the Riccati equation in the first hidden layer of neural network forward propagation, the trial functions are automatically generated, which leads to a simple and fast algebraic system. Our findings successfully offer an abundance of analytical solutions, including solitary waves that describe localized, stable wave pulses that propagate without deformation and periodic solutions that characterize oscillatory wave trains, which are often observed in shallow water flows, reservoir oscillations, and canal waves. These solutions offer valuable insight into wave steepening, dispersion, and energy redistribution in confined channels.

To help illustrate these wave features, we present a range of visual representations such as 3D, contours, and 2D plots, which provide further insight into how solitary and periodic waves transform under varying hydrodynamic conditions, particularly for applications such as navigating towards reservoirs for managed water storage, and water diversion through canals and spillways. The present study not only provides insights into analytical solution methods for sophisticated wave models but also sets the stage for future studies on nonlinear wave physics, coastal engineering, and reservoir–canal systems. Looking forward, there are three main suggestions: First, combine real-time sensor observations and sediment transport equations with the MGREMNN approach for optimal dam operation and reservoir cleaning. Second, extend the solver with deep reinforcement learning for water diversion and spillway flow regulation. Third, design open-source software using the MGREMNN approach to measure wave impacts on canals and levees for climate change adaptation and mitigation. Overall, this study is both a theoretical and practical foundation for future research, paving the way for better, safer, and more efficient management of water resources in natural and engineered systems.

Author Contributions: Q.-Y.S.: Conceptualization, supervision, methodology, project administration, writing—original draft preparation, validation. W.-F.F.: methodology, conceptualization, validation, writing—review and editing, supervision, project administration. All authors have read and agreed to the published version of the manuscript.

Funding: This research received no external funding.

Data Availability Statement: No new data were created or analyzed in this study. Data sharing is not applicable to this article.

Conflicts of Interest: The authors declare no conflicts of interest.

References

1. Amer, A.; Jaradat, E.K.; Rehman, H.U.; Abo-Dahab, S.M.; Hafez, R.M.; Yildirim, Y. Deciphering nonlinear wave phenomena in Einstein's vacuum field equation using analytical and numerical approaches. *Chaos Solitons Fractals* **2026**, *208*, 118371. [CrossRef]
2. Danladi, A.; Demirbilek, U.; Sulaiman, T.A.; Radwan, T.; Bulut, H.; Ahmed, K.K. Exploring fourth-order nonlinear integrable equation: Solitons, interactions and modulation instability. *J. Eng. Res.* **2026**, *14*, 2549–2559. [CrossRef]
3. Qawaqneh, H.; Tariq, K.U.; Alomair, A.; Alomair, M.A. Exploring the exact soliton solutions and modulation instability analysis of the (3+1)-dimensional oceanic wave model. *AIMS Math.* **2026**, *11*, 10936–10962. [CrossRef]
4. Christofides, P.D.; Chow, J. Nonlinear and robust control of PDE systems: Methods and applications to transport-reaction processes. *Appl. Mech. Rev.* **2002**, *55*, B29–B30. [CrossRef]
5. Schneider, G.; Uecker, H. *Nonlinear PDEs*; American Mathematical Society: Providence, RI, USA, 2017.
6. Kudryashov, N.A. Construction of nonlinear differential equations for description of propagation pulses in optical fiber. *Optik* **2019**, *192*, 162964. [CrossRef]
7. Shen, J.L.; Muhammad, J.; Younas, U. Investigating the wave dynamics and interaction structures: Exploring the Benney-Roskes/Zakharov-Rubenchik model in the oceanic atmosphere. *Ocean Eng.* **2026**, *354*, 124969. [CrossRef]
8. Younas, U.; Muhammad, J.; Murad, M.A.; Almutairi, D.K.; Khan, A.; Abdeljawad, T. Investigating the truncated fractional telegraph equation in engineering: Solitary wave solutions, chaotic and sensitivity analysis. *Results Eng.* **2025**, 104489. [CrossRef]
9. Murad, M.A.S. Analysis of optical soliton dynamics for the conformable Kudryashov equation by uniform method. *Eur. Phys. J. D.* **2026**, *80*, 42. [CrossRef]
10. Huang, J.; Wu, H. The neural network basis method for nonlinear partial differential equations and its Gauss–Newton optimizer. *Commun. Nonlinear Sci. Numer. Simul.* **2025**, *143*, 108608. [CrossRef]
11. Smaoui, N.; Al-Enezi, S. Modelling the dynamics of nonlinear partial differential equations using neural networks. *J. Comput. Appl. Math.* **2004**, *170*, 27–58. [CrossRef]
12. Zhang, H.; Huang, H. Neural network for solving nonlinear parabolic differential equations. *J. Phys. Conf. Ser.* **2022**, *2381*, 012050. [CrossRef]
13. Chen, X.; Peng, W.Q. PINN for solving forward and inverse problems involving integrable two dimensional nonlocal equations. *Commun. Theor. Phys.* **2025**, *77*, 025002. [CrossRef]
14. Abraham, A. Meta learning evolutionary artificial neural networks. *Neurocomputing* **2004**, *56*, 1–38. [CrossRef]
15. Höffgen, K.U. Computational limitations on training sigmoid neural networks. *Inf. Process. Lett.* **1993**, *46*, 269–274. [CrossRef]
16. Shen, J.; Li, X. Solving the exact solutions of the fifth-order dispersive Caudrey-Dodd-Gibbon equation based on the feature-enhanced direct symbolic computation neural network algorithm. *Nonlinear Dyn.* **2026**, *114*, 809. [CrossRef]
17. Shen, J.; Zhang, R.; Huang, J.; Liang, J. Neural network-based symbolic computation algorithm for solving (2+1)-dimensional Yu-Toda-Sasa-Fukuyama equation. *Mathematics* **2025**, *13*, 3006. [CrossRef]
18. Liang, J.; Shen, J.; Deng, G. Investigation of multiple soliton solutions for high-dimensional models using automatic logarithmic bilinear transformation. *Ocean Eng.* **2026**, *368*, 128374. [CrossRef]
19. Yuan, S.; Liu, Y.; Yan, L.; Zhang, R.; Wu, S. Neural networks-based analytical solver for exact solutions of fractional partial differential equations. *Fractal Fract.* **2025**, *9*, 541. [CrossRef]
20. Ablowitz, M.J.; Clarkson, P.A. *Solitons, Nonlinear Evolution Equations and Inverse Scattering*; Cambridge University Press: Cambridge, UK, 1991.
21. Fang, K.; Liu, Z.; Wang, P.; Wu, H.; Sun, J.; Yin, J. Modeling solitary wave propagation and transformation over complex bathymetries using a two-layer Boussinesq model. *Ocean Eng.* **2022**, *265*, 112549. [CrossRef]
22. Mohammed, W.W.; Alshammary, M.W.; Matouk, A.E.; Iqbal, N. Abundant solitary solutions for the fractional unidirectional wave model using in oceanography, coastal engineering, and meteorology. *Eur. J. Pure Appl. Math.* **2025**, *18*, 6422. [CrossRef]
23. Biazar, J.; Babolian, E.; Islam, R. Solution of the system of ordinary differential equations by Adomian decomposition method. *Appl. Math. Comput.* **2004**, *147*, 713–719. [CrossRef]
24. Younas, U.; Hussain, E.; Muhammad, J.; Sharaf, M.; Meligy, M.E. Chaotic Structure, Sensitivity Analysis and Dynamics of Solitons to the Nonlinear Fractional Longitudinal Wave Equation. *Int. J. Theor. Phys.* **2025**, *64*, 42. [CrossRef]
25. Hashemi, M.S.; Baleanu, D. *Lie Symmetry Analysis of Fractional Differential Equations*; Chapman and Hall/CRC: Boca Raton, FL, USA, 2020.
26. Ai, W.; Zeng, J.; Jianli, F.; Lei, Z. Bifurcation analysis and control of traffic flow model considering the impact of smart devices for drivers. *J. Comput. Nonlinear Dyn.* **2025**, *20*, 041005. [CrossRef]

27. Muhammad, J.; Younas, U.; Ahmed, K.K. Investigating higher-dimensional nonlinear evolution equation: Dynamics of waves and multistability in fluid mediums. *Model. Earth Syst. Environ.* **2025**, *11*, 442. [CrossRef]
28. Kopçasız, B. Unveiling new exact solutions of the complex-coupled Kuralay system using the generalized Riccati equation mapping method. *J. Math. Sci. Model.* **2024**, *7*, 146–156. [CrossRef]
29. Wang, J.; Liu, Y.; Yan, L.; Han, K.; Feng, L.; Zhang, R. Fractional sub-equation neural networks (fSENNs) method for exact solutions of space–time fractional partial differential equations. *Chaos An. Interdiscip. J. Nonlinear Sci.* **2025**, *35*, 1–17. [CrossRef]
30. Kumar, S.; Hamid, I.; Abdou, M.A. Dynamic frameworks of optical soliton solutions and soliton-like formations to Schrödinger–Hirota equation with parabolic law non-linearity using a highly efficient approach. *Opt. Quantum Electron.* **2023**, *55*, 1261. [CrossRef]
31. Younas, U.; Muhammad, J.; Hussain, E. Higher dimensional nonlinear model arising to the diversity of fields: Dynamics of wave structures with -fractional derivative. *Partial Differ. Equ. Appl. Math.* **2025**, *16*, 101284. [CrossRef]
32. Dhiman, S.; Kumar, S. Analyzing specific waves and various dynamics of multi-peakons in (3+1)-dimensional p-type equation using a newly created methodology. *Nonlinear Dyn.* **2024**, *112*, 1–14. [CrossRef]
33. Nadeem, M.; Arqub, O.A.; Ali, A.H.; Neamah, H.A. Bifurcation, chaotic analysis and soliton solutions to the (3+1)-dimensional p-type model. *Alex. Eng. J.* **2024**, *107*, 245–253. [CrossRef]
34. Mohan, B.; Kumar, S.; Kumar, R. Higher-order rogue waves and dispersive solitons of a novel P-type (3+1)-D evolution equation in soliton theory and nonlinear waves. *Nonlinear Dyn.* **2023**, *111*, 20275–20288. [CrossRef]
35. Senol, M.; Erol, M.O. New conformable P-type (3+1) dimensional evolution equation and its analyical and numerical solutions. *J. New Theory* **2024**, *46*, 71–88. [CrossRef]

Disclaimer/Publisher's Note: The statements, opinions and data contained in all publications are solely those of the individual author(s) and contributor(s) and not of MDPI and/or the editor(s). MDPI and/or the editor(s) disclaim responsibility for any injury to people or property resulting from any ideas, methods, instructions or products referred to in the content.